A novel higher-order finite element framework for the process modeling of material extrusion additive manufacturing

Manish H. Nagaraj*, Marianna Maiaru†
Department of Mechanical Engineering,
University of Massachusetts Lowell, MA 01854, United States

Manuscript

Corresponding Author:
Marianna Maiaru,
Associate Professor,
Department of Mechanical Engineering,
University of Massachusetts Lowell,
Lowell 01854,
MA, United States.
e-mail: marianna_maiaru@uml.edu

*Postdoctoral Research Associate, e-mail: manish_nagaraj@uml.edu
†Associate Professor, e-mail: marianna_maiaru@uml.edu

Abstract

Material extrusion additive manufacturing enables the rapid fabrication of complex structures for a wide range of applications, including within the aerospace and healthcare sectors. Optimizing the performance of additively manufactured polymer structures depends on the ability to predict residual stress induced by the sequential solidification of the extruded layers. Self-equilibrated residual stresses are influenced by the thermal history of the part during the manufacturing process. This work introduces a novel numerical framework for the process modeling of material extrusion additive manufacturing. The numerical modeling is based on higher-order finite elements derived from the Carrera Unified Formulation (CUF), which enables accurate prediction of the stress field while reducing the associated computational overheads. Element activation is adopted to model the evolving structure during material extrusion and deposition. Heat exchange mechanisms such as conduction (filament/filament, filament/build platform), convection, and radiation are included in the model. A transient thermal analysis is performed in this new framework to predict the temperature distribution within the part during its fabrication. Multiple numerical assessments are presented for the material extrusion additive manufacturing of parts ranging in size from 30 mm to over 1500 mm. The predicted thermal profiles are in excellent agreement with reference experimental observations, thereby validating the proposed numerical framework and demonstrating its capability to model the printing process accurately. Results from this work are a milestone toward optimizing additively manufactured polymer parts.

Keywords: Material extrusion additive manufacturing, thermal modeling, higher-order finite elements

1 Introduction

Additive Manufacturing (AM) is an emerging processing technology that has gained significant prominence over the past two decades for its capability in fabricating complex parts whose geometries are beyond that of conventional manufacturing techniques [1]. Material extrusion additive manufacturing [2], commonly referred to as Fused Filament Fabrication (FFF), is one of the most popular forms of AM wherein a molten thermoplastic filament is extruded through a moving nozzle and deposited along a predefined path, thereby creating the required geometry. Because of its capabilities, the FFF processing technique has been adopted for a diverse range of applications within the automotive, aerospace, and medical device industries [3].

FFF involves high-temperature gradients within the printed component as it undergoes rapid heating due to the deposition of the semi-molten material and subsequently cools down via heat transfer with adjacent layers and the environment [4]. The resulting temperature gradients can lead to the development of residual stresses within the manufactured component, which impacts both its dimensional accuracy as well as mechanical performance [5–8]. Processing conditions direct the evolution of material properties in polymer-based material systems [9–15], and can subsequently influence the mechanical response of the fabricated component [16–18]. In the case of FFF, the changes in temperature during the heating and cooling phases influences the crystalline morphology (microstructure) of the thermoplastic material, which significantly affects its mechanical properties [19, 20]. Consequently, the temperature distribution within the printed part during its processing drives its geometrical shape and mechanical performance. The thermal profile of a printed component is a function of process parameters, such as filament extrusion temperature and deposition path, print speed, and the ambient environmental state [21, 22]. These process parameters can be optimized to induce thermal profiles with minimal variations to limit residual stresses and, in turn, ensure optimal print quality and mechanical performance over the component's service life. Optimizing FFF process parameters through trial-error experimental approaches is inefficient in terms of cost and lead times due to the large number of involved parameters [23, 24]. Therefore, virtual testing methodologies are becoming the preferred approach for process optimization [25, 26].

Costa et al. investigated the heat transfer mechanisms relevant to FFF to develop guidelines for numerical modeling [4]. Some early 3D models based on the Finite Element Method (FEM) for process simulation were proposed by Zhang and Chou [27, 28]. Considering the importance of accurately predicting the thermal profile during the printing process, several numerical approaches have been proposed in the literature to model heat transfer during FFF process modeling [29–37]. In recent years, 3D-FE models have also been developed to investigate the influence of FFF thermal state on residual stress development and part distortion [5, 6, 38]. However, traditional physics-based numerical techniques to model the FFF process often incur high computational costs due to the need to model each deposition layer, limiting the capability to establish digital twins [32, 39]. The significant limitations of traditional FE approaches become even more relevant for large-scale structures 3D-printed via Big Area Additive Manufacturing (BAAM), which requires the deposition of hundreds of layers [40–42]. Recent investigations have proposed alternative numerical models for FFF simulation to

reduce computational overheads. Owens et al. proposed a scalable 2D finite volume model to simulate thermal histories for FFF and BAAM processes rapidly [43]. Roy and Wodo recently developed a data-driven surrogate model for the thermal modeling of AM processes [44].

This work establishes a novel and computationally efficient numerical framework to model material extrusion-based additive manufacturing processes, which can be used to optimize process parameters for FFF. The computational model is based on higher-order finite elements and is developed using the Carrera Unified Formulation (CUF) [45]. CUF is a hierarchical mathematical framework capable of deriving structural theories of any polynomial order which, combined with 1D and 2D finite elements, leads to a 3D modeling approach whose accuracy is comparable to that of traditional 3D-FE models at significantly reduced computational cost [46]. CUF models have been successfully employed in various applications such as contact modeling [47], progressive damage and impact analysis of composite structures [48–50], and the micromechanical modeling and analysis of fiber-reinforced polymer composites [51, 52]. CUF models have also been successfully combined with the global-local technique for computationally efficient nonlinear structural analysis [53–55]; however, its potential has never been explored for 3D printing process modeling. The present work proposes a CUF-based numerical framework where Lagrange polynomial expansions are implemented to model the FFF and BAAM processes and to predict the evolving thermal profile of the 3D-printed part.

The organization of this article is as follows: Section 2 describes the numerical modeling approach for the process modeling of material extrusion additive manufacturing. A series of numerical assessments are presented in Section 3 as validation cases compared to experimental data, and the main conclusions are summarized in Section 4.

2 Computational Methods

This section provides an overview of the higher-order finite element approach used in the present work, and the modeling techniques adopted for AM simulation and thermal analysis.

2.1 Higher-order structural modeling

Structural modeling in the proposed numerical framework is based on higher-order structural theories derived using the Carrera Unified Formulation and implemented using the Finite Element Method [45]. In thisapproach, additional 2D interpolation terms – known as Expansion functions F_τ – are employed to improve the kinematics of 1D finite elements (B2 and B3 beam elements with 2 and 3 nodes, respectively), respectively, as shown in Fig. 1, and are are defined over the 1D element cross-section. This mathematical representation results in a 3D description of the displacement field, leading to numerical solutions comparable to 3D-FE models in accuracy but with significantly reduced computational effort [46]. A brief overview of 1D-CUF and its extension to model time-dependent property evolutions for 3D printing is presented hereinafter.

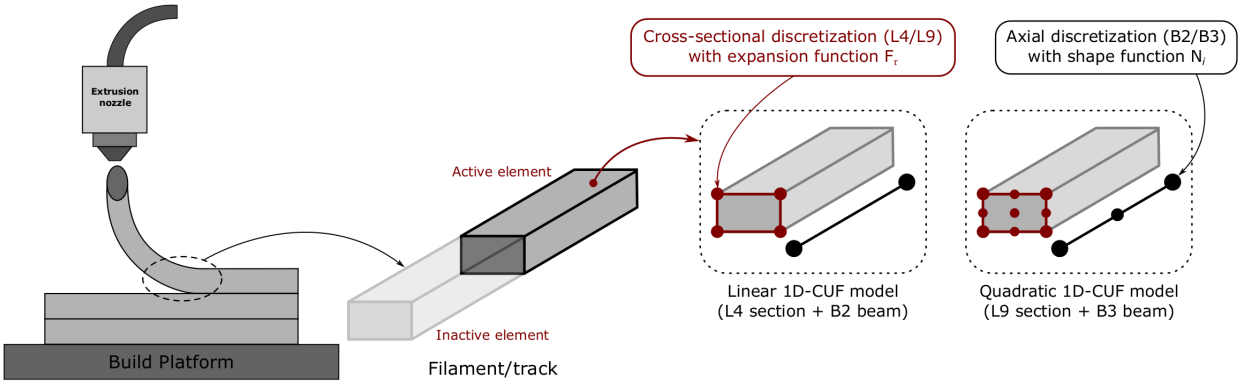

Figure 1: 1D-CUF modeling of the deposited filament track for additive manufacturing simulation.

Considering the 1D-CUF model shown in Fig. 1, the displacement field $\mathbf{u}$ is defined as

$$\mathbf{u} = F_\tau(x,z)\mathbf{u}_\tau(y),\ \tau = 1,2,...,M \tag{1}$$

where M is the number of terms within the expansion function F_τ and $\mathbf{u}_\tau$ represents the generalized displacements. Expansion functions based on Lagrange polynomials are used in the present work, and are implemented in the form of 2D quadrilateral elements as shown in Fig. 1 (L4 and L9 section elements with 4 and 9 nodes, respectively). This allows for the explicit modeling of the beam cross-section, and results in the Component-Wise modeling approach [56, 57].

Finite element formulation

The stress and strain fields are defined as

$$\begin{aligned} \boldsymbol{\sigma} &= \{\sigma_{xx}, \sigma_{yy}, \sigma_{zz}, \sigma_{xy}, \sigma_{xz}, \sigma_{yz}\} \\ \boldsymbol{\varepsilon} &= \{\varepsilon_{xx}, \varepsilon_{yy}, \varepsilon_{zz}, \varepsilon_{xy}, \varepsilon_{xz}, \varepsilon_{yz}\} \end{aligned} \tag{2}$$

The linear displacement-strain relationship is given by

$$\boldsymbol{\varepsilon}(t) = \mathbf{D}\mathbf{u}(t) \tag{3}$$

where (t) indicates a dependency on time due to the printing process. The differentiation operator $\mathbf{D}$ is defined as

$$\mathbf{D} = \begin{bmatrix} \frac{\partial}{\partial x} & 0 & 0 \\ 0 & \frac{\partial}{\partial y} & 0 \\ 0 & 0 & \frac{\partial}{\partial z} \\ \frac{\partial}{\partial y} & \frac{\partial}{\partial x} & 0 \\ \frac{\partial}{\partial z} & 0 & \frac{\partial}{\partial x} \\ 0 & \frac{\partial}{\partial z} & \frac{\partial}{\partial y} \end{bmatrix}$$

The constitutive relation is

$$\boldsymbol{\sigma}(t) = \mathbf{C}(t)\boldsymbol{\varepsilon}(t) \tag{4}$$

where the material stiffness tensor is denoted by the 6×6 $\mathbf{C}$ matrix, and evolves as a function of time due to changes in the material properties during the processing phase. Defining the displacement field in terms of the finite element shape functions $N_i(y)$ and the cross-sectional expansion functiions $F_\tau(x, z)$ leads to the following 3D form

$$\mathbf{u}(x, y, z) = F_\tau(x, z)N_i(y)\mathbf{u}_{\tau i} \tag{5}$$

where i and τ are nodal indices for the 1D finite element and 2D sectional element, respectively. According to the principle of virtual work

$$\delta L_{int} = \delta L_{ext} \tag{6}$$

where δL_{int} is the virtual variation of the internal strain energy and is defined as

$$\delta L_{int} = \int_V \delta\boldsymbol{\varepsilon}^T : \boldsymbol{\sigma} \tag{7}$$

Combining Eqs. 4, 5 and 7, Eq. 6 can be written as

$$\delta L_{int} = \delta\mathbf{u}_{sj}^T \mathbf{k}_{ij\tau s}\mathbf{u}_{\tau i} \tag{8}$$

where $\mathbf{k}_{ij\tau s}$ is

$$\mathbf{k}_{ij\tau s} = \int_l \int_A \mathbf{D}^T(N_i(y)F_\tau(x, z))\mathbf{C}\mathbf{D}(N_j(y)F_s(x, z))\ dA\ dl \tag{9}$$

Equation 9 represents a 3x3 matrix, termed the Fundamental Nucleus (FN), whose definition remains invariant with respect to the choice of finite element and expansion function used to derive the structural theory. Assembling the structural FN over the nodal indices $\{i, j, \tau, s\}$ results in the element stiffness matrix, which can

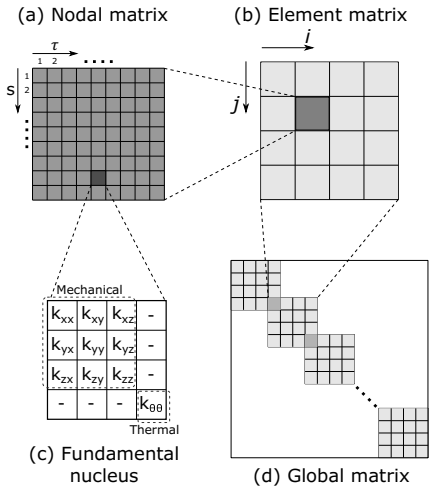

Figure 2: Assembly of global matrices using Fundamental Nuclei in CUF.

subsequently be assembled to develop the global stiffness matrix as seen schematically in Fig. 2.

2.2 Process simulation with element activation

The evolution of the printed domain that occurs due to continuous material deposition in FFF needs to be modeled to represent the additive manufacturing process accurately. A popular approach to model the evolving structural domain is via the element activation strategy, e.g., Ref [5], which is adopted in this work. Element activation is combined with a voxelization technique, wherein the physical structure is modeled using cuboidal finite elements [58], as shown in Fig. 3 for the case of an 'L-shaped' structural domain.

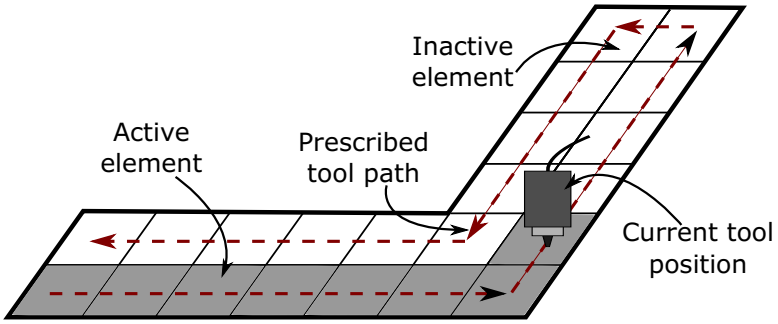

Figure 3: Element activation strategy to simulate the FFF deposition process.

In this approach, a finite element model of the entire structure is developed, and each element is initially set to be deactivated, i.e., the element does not transfer thermal or mechanical loads. During the time-based analysis, the tool's current position (extruder) is computed based on input parameters such as print velocity, current time, and the prescribed tool path. The relevant information is obtained from the G-code data associated with the specific printed geometry. Once the current tool position is evaluated, a check is performed to identify the elements through which the tool traverses with respect to its position at the previous time step, and the elements thus identified are activated, i.e., the tool-path is traced along the finite element model, and elements are activated according to the tool traversal between consecutive time-steps.

2.3 Heat transfer mechanisms

The thermal profile of a component fabricated via FFF depends on the printed part's thermal interactions with the extrusion nozzle, build platform, and the surrounding environment [4]. A schematic view of the relevant heat transfer mechanisms is shown in Fig. 4.

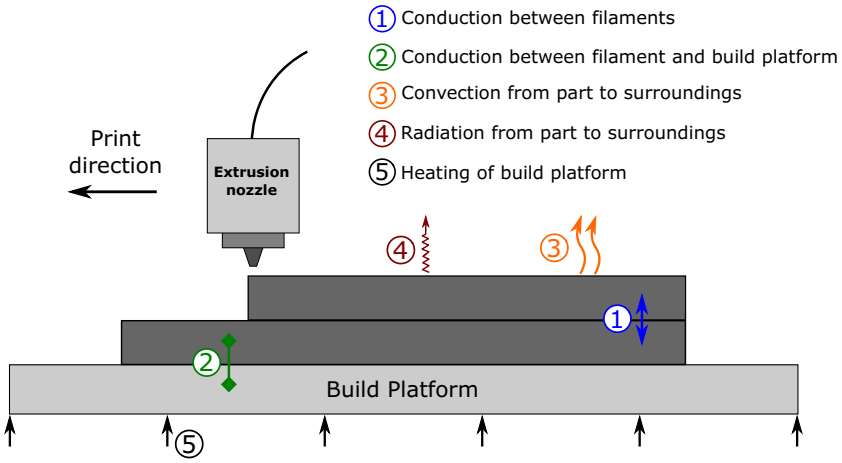

Figure 4: Heat transfer mechanisms active during the FFF process and modeled within the proposed framework.

Heating occurs due to the deposition of the molten filament at elevated temperatures, while cooling occurs due to heat loss from the external surfaces of the structure to the surroundings via convection and radiation. Heat is transferred within a deposited filament and between consecutive layers via conduction. The part also interacts with the build platform through heat conduction, as shown in Fig. 4. These mechanisms and environmental factors, such as the presence of a heated print chamber or cooling fans, determine the temperature distribution within the printed domain. In the present work, all the aforementioned thermal mechanisms are accounted for during the FFF simulation by updating the numerical model's thermally available volume and surface area, which evolve according to the set of activated elements within a time step. A simple two-element model is schematically shown in Fig. 5 to illustrate the heat exchange mechanisms modeled.

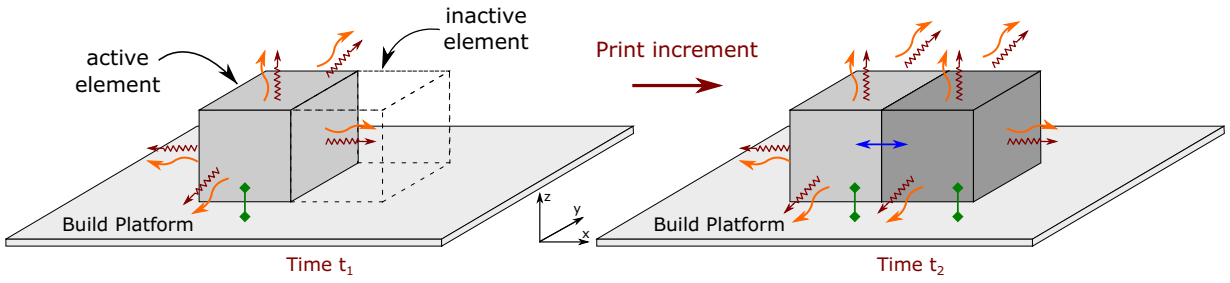

Figure 5: Evolution of structural domain to implement the heat transfer mechanisms induced by FFF.

In Fig. 5, a single element is initially active at time t_1. Therefore, cooling occurs via convection and radiation from the side and top faces, whereas conduction is responsible for interactions between the element and the build platform via the bottom face. The adjacent element is activated in a subsequent time step, time t_2. The shared face between the two elements, earlier an external surface area, is now interior to the structure and,

therefore, no longer available for convection and radiation. Conduction through this shared face is responsible for the thermal interaction between the two elements in the current configuration. The remaining element faces exposed to the environment allow convective and radiative heat loss while the bottom faces conduct heat with the build platform, as shown in Fig. 5 at time t_2.

2.4 Transient thermal analysis

The temperature distribution within the printed domain evolves with time as molten filament is continuously deposited. An accurate evaluation of the temperature gradients and thermal state during printing requires the quantification of the relevant heat transfer mechanisms depicted in Fig. 4. A transient thermal analysis is performed to determine the thermal state within the printed domain [5, 6]

$$\rho c_p \frac{\delta T}{\delta t} = \nabla \cdot (\kappa \nabla T) \tag{10}$$

where ρ, c_p and κ represent the density, specific heat capacity, and thermal conductivity of the deposited filament, respectively, and T is the temperature. The temperature of newly deposited material at time t is specified as an initial condition

$$T(\mathbf{x}, t) = T_{deposition},\ \mathbf{x} \in \Omega_{deposition} \tag{11}$$

where $T_{deposition}$ is the deposition temperature and $\Omega_{deposition}$ is the domain of the deposited material. The build platform temperature is specified as a boundary condition

$$T(\mathbf{x}) = T_{platform},\ \mathbf{x} \in \Omega_{platform} \tag{12}$$

where $T_{platform}$ is the temperature of the build platform $\Omega_{platform}$. The boundary conditions of the deposited domain are defined as

$$\kappa \frac{\delta T}{\delta \mathbf{n}} + q_c + q_r = 0,\ \mathbf{x} \in S(t) \tag{13}$$

where $S(t)$ is the evolving external surface of the deposited domain (see Fig. 5) with $\mathbf{n}$ denoting its outward normal vector. The convective heat flux q_c and radiative heat flux q_r are evaluated as follows

$$q_c = h(T - T_{ambient}) \tag{14}$$

$$q_r = \sigma\epsilon(T^4 - T^4_{ambient}) \tag{15}$$

where h and ϵ are the convective heat transfer coefficient and emissivity of the material, respectively. σ is the Stefan–Boltzmann constant, and $T_{ambient}$ is the ambient temperature.

The numerical solution of the transient thermal problem requires the discrete form of the heat transfer equation as follows

$$\mathbf{M}\dot{\mathbf{T}} + \mathbf{K}\mathbf{T} = \mathbf{F} \tag{16}$$

where $\mathbf{M}$ is the thermal capacitance matrix, and $\mathbf{F}$ denotes the thermal loads. $\mathbf{K}$ represents the thermal stiffness matrix and includes conductive, convective, and radiative contributions [59]. Applying the Backward Euler approach to Eq. 16

$$\mathbf{M}\left(\frac{\mathbf{T}_{n+1} - \mathbf{T}_n}{\Delta t}\right) + \mathbf{K}\mathbf{T}_{n+1} = \mathbf{F}_{n+1} \tag{17}$$

Rearranging the above leads to

$$\left(\frac{\mathbf{M}}{\Delta t} + \mathbf{K}\right)\mathbf{T}_{n+1} = \left(\frac{\mathbf{M}}{\Delta t}\right)\mathbf{T}_n + \mathbf{F}_{n+1} \tag{18}$$

Equation 18 is solved to obtain the evolving temperature field within the extant structure during the printing process. Within the CUF modeling approach (see Section 2.1), the fundamental nuclei, required for the assembly of $\mathbf{M}$ and $\mathbf{K}$ matrices, are respectively as follows [45, 60]

$$\mathbf{m}_{ij\tau s} = \rho \int_l \int_A N_i(y)F_\tau(x,z) \cdot N_j(y)F_s(x,z)\ dA\ dl \tag{19}$$

$$\mathbf{k}_{ij\tau s} = \kappa \int_l \int_A \boldsymbol{\nabla}^T(N_i(y)F_\tau(x,z)) \cdot \boldsymbol{\nabla}(N_j(y)F_s(x,z))\ dA\ dl \tag{20}$$

3 Results and Discussion

This section presents a set of experimentally validated numerical studies to evaluate the performance of the proposed framework for AM simulation. Results are presented in terms of evolving temperature fields of the printed component under the influence of FFF and BAAM processing conditions.

3.1 Modeling of a single-filament wall

The numerical assessment considered herein is the FFF process modeling of a printed wall with a single-filament thickness, schematically shown in Fig. 6. The selected case is based on the work of Lepoivre et al. [34], which

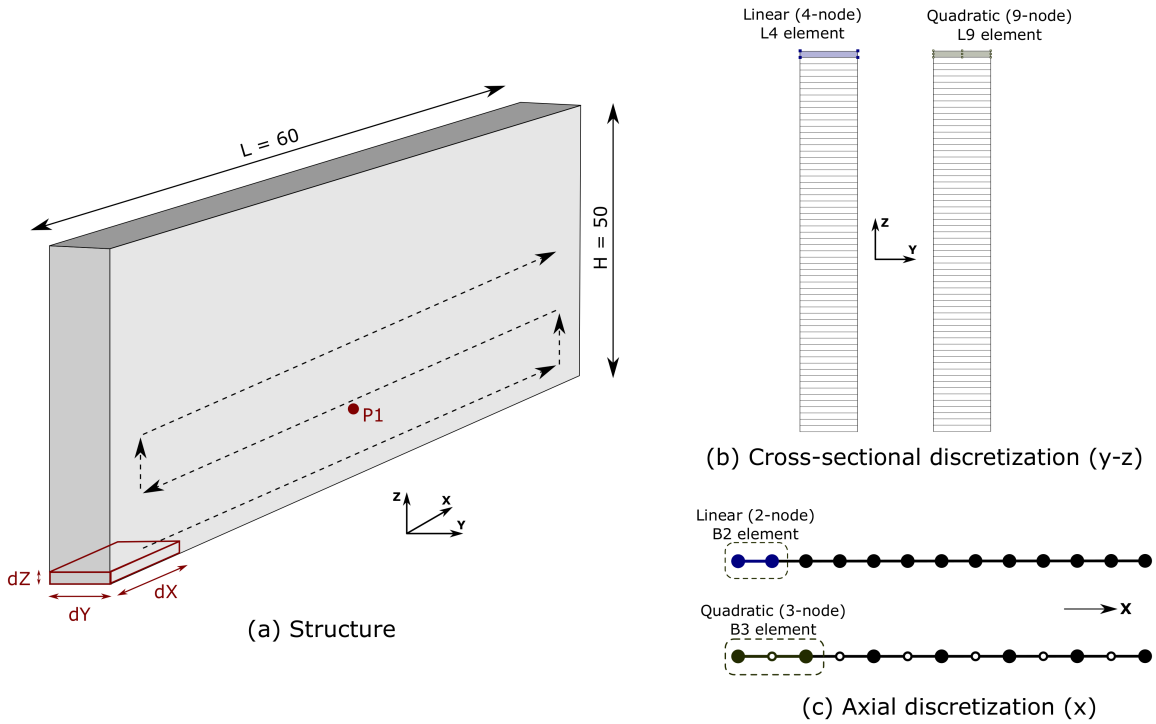

Figure 6: Schematic representation of (a) the single-filament wall (dimensions in mm). The dashed lines indicate the tool travel path, and the highlighted $dX \times dY \times dZ$ voxel domain represents an individual finite element, (b) the linear and quadratic cross-section discretization, and (c) the linear and quadratic axial discretization used in the numerical analysis.

Table 1: Thermal properties of the materials used in the numerical modeling of the single-wall [34].

Property	ABS	PEKK	build platform
Density $[kg/m^3]$	1050.0	1140.0	2210.0
Thermal conductivity $[W/mK]$	0.2	0.5	1.4
Specific heat capacity $[J/kgK]$	2100.0	2200.0	730.0
Emissivity ε	0.91	0.94	–
Filament width (dY) [mm]	1.25	2.20	–
Filament thickness (dZ) [mm]	0.80	0.80	–

provides experimental reference data and numerical solutions. The present analysis aims to conduct an initial verification and validation of the proposed numerical framework for FFF process modeling. The thermoplastic filament is composed of Acrylonitrile butadiene styrene (ABS), with a filament thickness (dZ) and width (dY) of 0.8 mm and 1.25 mm, respectively. The voxelized numerical model, therefore, consists of finite elements of dimensions $dX \times\ 1.25\ mm \times\ 0.8\ mm$, where dX is the finite element length along the filament direction. The thermal properties of the ABS filament and the build platform are listed in Table 1. The process parameters used in the analysis are summarized in Table 2.

A series of linear and quadratic CUF models have been developed by progressively refining the mesh along the filament direction, i.e., decreasing the 1D element length dX as shown in Fig. 6. A single sectional element (with dimensions $dY \times dZ$) is used to represent the filament cross-section. The temperature profile at the midspan of Layer-6, i.e., the point P1 (30, 0, 4.4) (refer to Fig. 6), as predicted by the linear and quadratic

Table 2: FFF process parameters used in the numerical modeling of the single-wall [34].

Parameter	ABS	PEKK
Extrusion temperature $[°C]$	255.0	356.0
Chamber temperature $[°C]$	95.0	139.0
build platform temperature $[°C]$	100.0	160.0
Convection coefficient $[W/m^2K]$	30.0	30.0
Print velocity $[mm/s]$	6.741	6.12

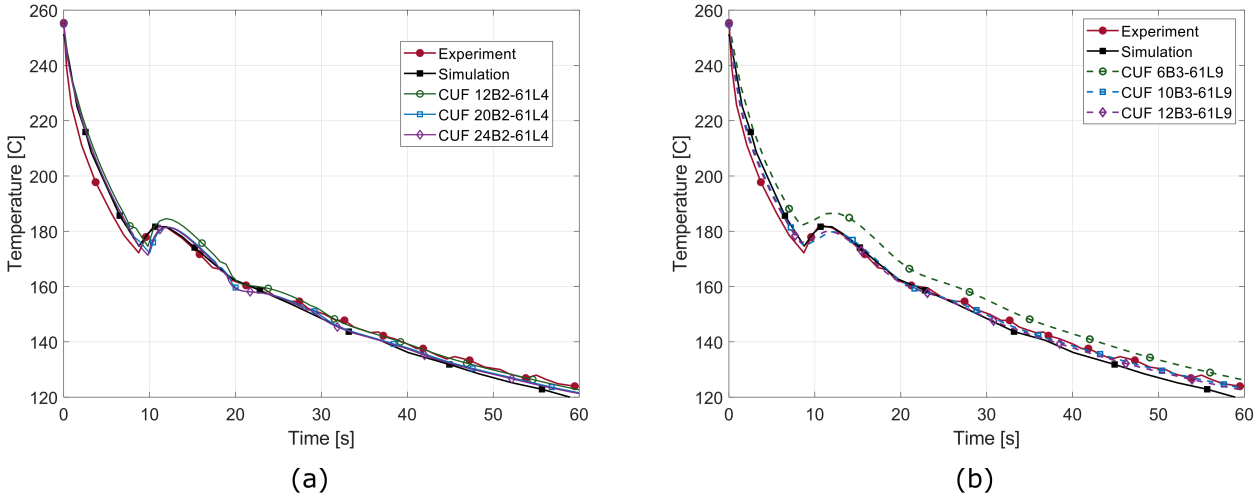

Figure 7: Thermal profile of the ABS single-filament wall as predicted by (a) the linear CUF models, and (b) the quadratic CUF models. Reference experimental and numerical data obtained from [34].

CUF models, is plotted in Fig. 7 (a) and (b), respectively. Reference experimental measurements and FE-based numerical predictions are also overlaid in the figure for comparison. A summary of the CUF models is provided in Table 3.

The temperature evolution within a single-wall structure printed using high melting-point thermoplastics such as PEKK ($T_{deposition} = 356\ °C$) was also experimentally investigated by Lepoivre et al. [34], and has been modeled in this work. This study aims to assess the model performance under high-temperature processing conditions. The PEKK material properties and process parameters are listed in Table 1 and Table 2, respectively. The CUF models used in the previous case (with ABS filament), as listed in Table 3, are retained for the FFF process modeling of the PEKK single-wall. The thermal profile predicted by the linear and quadratic CUF

Table 3: Summary of CUF models used in the single-wall thermal analysis.

Model	Discretization	Beam length (dX) [mm]	DOF
CUF - Linear 1	12 B2, 61 L4	5.0	1,612
CUF - Linear 2	20 B2, 61 L4	3.0	2,604
CUF - Linear 3	24 B2, 61 L4	2.5	3,100
CUF - Quadratic 1	6 B3, 61 L9	10.0	4,797
CUF - Quadratic 2	10 B3, 61 L9	6.0	7,749
CUF - Quadratic 3	12 B3, 61 L9	5.0	9,225

models at the midspan of Layer-6, P1 (30, 0, 4.4), with reference experimental and numerical data overlaid for comparison, is shown in Fig. 8. The temperature distribution over the PEKK single-wall at various stages of the printing process, as predicted by the 'CUF - Linear 2' model, is shown in Fig. 9.

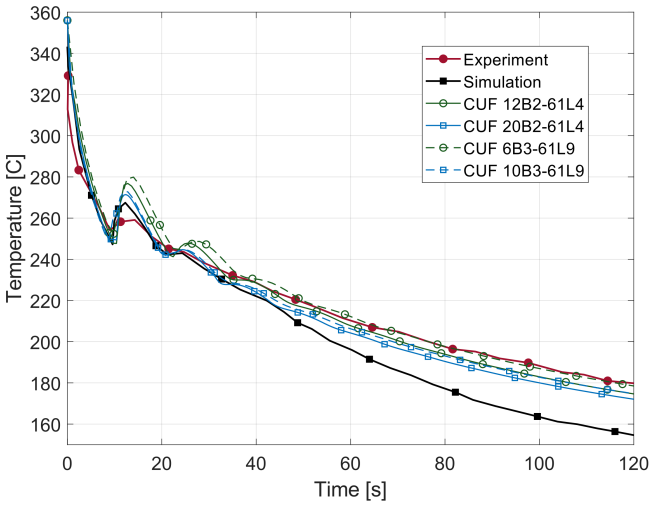

Figure 8: Thermal profile of the PEKK single-filament wall as predicted by the CUF models. Reference experimental and numerical data obtained from [34].

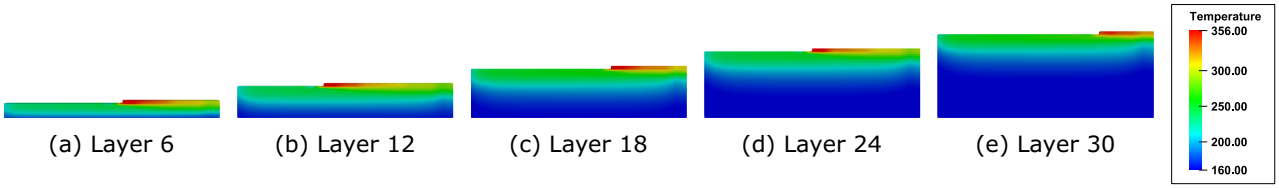

Figure 9: Temperature distribution of the PEKK single-filament wall at various stages of print as predicted by the 'CUF - Linear 2' model.

It is seen from the predicted thermal profiles of the ABS single-wall, plotted in Fig. 7, that the CUF models are in excellent agreement with both experimental measurements and the reference numerical results. The mesh convergence analysis for both linear and quadratic CUF models indicates the coarsest discretization, i.e., the 'CUF - Linear 1' and the 'CUF - Quadratic 1' models slightly overestimate the temperature. In contrast, the more refined numerical models lead to an accurate evaluation of the temperature state. This case study provides an initial verification and validation of the proposed CUF-based numerical framework for FFF process modeling and transient thermal analysis.

Similarly, the CUF predictions for the case of the PEKK single-wall are also in excellent agreement with experimental data, as evidenced in Fig. 8. This is in contrast to the numerical results provided by the original study, which deviate from the experimental curve after approximately 40 seconds of the simulated time. The accuracy of the CUF predictions is explained by the fact that the modeling approach is fully 3D in nature, while that of the reference simulation is based on a 2D-FE model, and can therefore model surface heat transfer mechanisms more accurately. The results in Fig. 7 and Fig. 8 demonstrate the capability of CUF models in modeling FFF over a wide range of processing temperatures.

Table 4: PLA material properties used in the open-box analysis [6, 37].

Property	PLA
Density $[kg/m^3]$	1250.0
Thermal conductivity $[W/mK]$	0.195
Specific heat capacity $[J/kgK]$	1950.0
Emissivity ε	0.78
Filament width (dY) [mm]	1.0
Filament thickness (dZ) [mm]	0.6

Table 5: FFF process parameters used in the open-box analysis [37].

Parameter	PLA
Extrusion temperature $[°C]$	200.0
Chamber temperature $[°C]$	25.0
build platform temperature $[°C]$	25.0
Convection coefficient $[W/m^2K]$	8.5
Print velocity $[mm/s]$	5.0

3.2 Modeling of an open-box

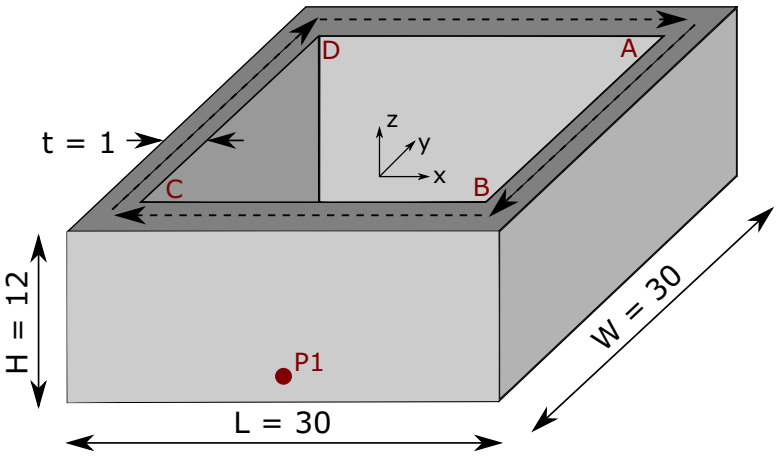

Figure 10: Schematic representation of the open-box structure with dashed lines indicating the tool travel path (dimensions in mm).

This numerical assessment models the FFF processing of an open box, i.e., a box without the top and bottom faces. The structure and test setup are based on the works of Zhang et al. [37, 61], which provide reference experimental and numerical data. A schematic representation of the printed structure is shown in Fig. 10. The structure is printed using polylactic acid (PLA) filaments of width 1.0 mm and height 0.6 mm. The PLA material properties, obtained from Trofimov et al. [6], are used in the present analysis and are reported in Table 4. The FFF process parameters are summarized in Table 5.

As in the previous case, a series of linear and quadratic CUF models, with an incremental refinement of the voxelized filament length (dX), has been used in the analysis. A single Lagrange sectional element of dimensions $dY \times dZ$ is used to model the filament cross-section. The CUF model predictions of the temperature profile at

point P1 (15.0, 30.0, 0.9), i.e., the center of Layer-2 in the open-box side BC (refer Fig. 10), are plotted in Fig. 11. Experimental measurements and numerical predictions from Zhang et al. [37, 61] have also been compared. The temperature distribution of the structure at various stages of print is visualized in Fig. 12. A summary of the CUF models is presented in Table 6.

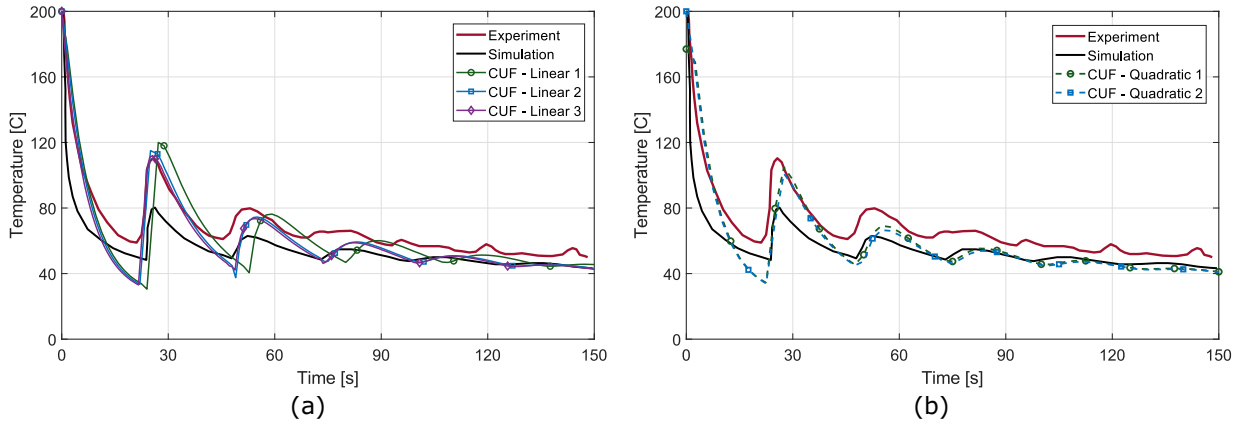

Figure 11: Thermal profile of the PLA open-box as predicted by (a) the linear CUF models, and (b) the quadratic CUF models. Reference experimental and numerical data obtained from Zhang et al. [37, 61].

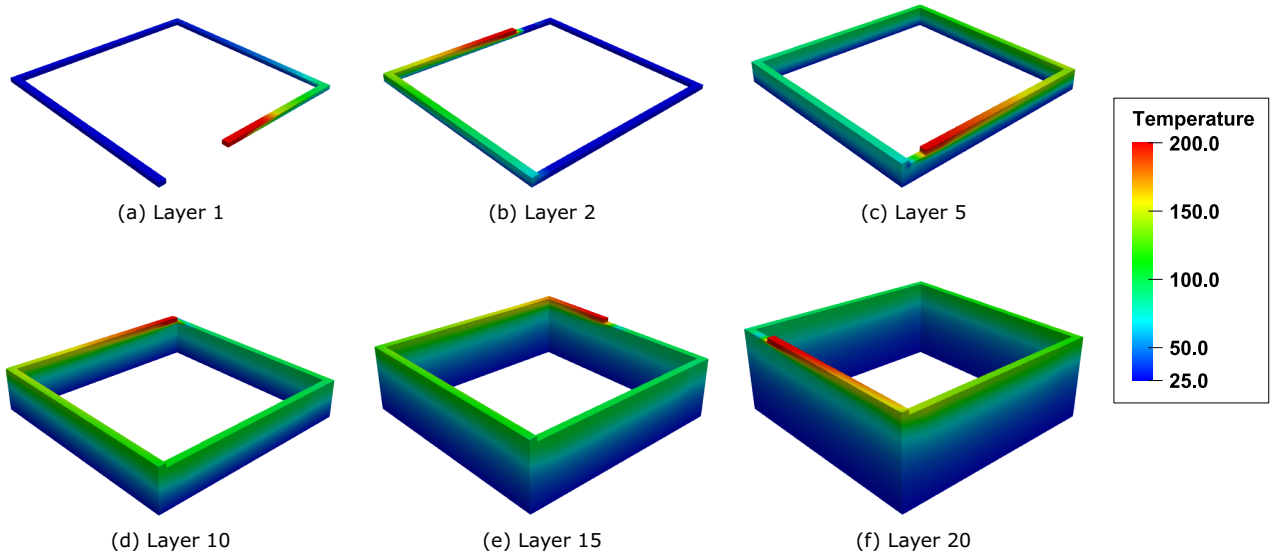

Figure 12: Temperature distribution of the open-box at various stages of print as predicted by the 'CUF - Linear 3' model.

It is seen from Fig. 11 that all the CUF model predictions (apart from the coarsest 'CUF - Linear 1' model) are in good general agreement with the experimental reference data and perform better than the reference simulation results while capturing the secondary temperature peaks arising from subsequent layer deposition. The discrepancy between the numerical and experimental curves is attributed to the sensitivity of the temperature field to the thermal properties considered in the analysis [37]. Section 3.3 presents a further investigation of the sensitivity of the thermal analysis to variations in material properties.

Table 6: Summary of CUF models used in the open-box thermal analysis.

Model	Discretization	Beam length (dX) [mm]	DOF
CUF - Linear 1	8 B2, 168 L4	4.67	1,870
CUF - Linear 2	12 B2, 252 L4	2.80	2,310
CUF - Linear 3	14 B2, 294 L4	2.33	2,530
CUF - Quadratic 1	6 B3, 126 L9	7.00	5,307
CUF - Quadratic 2	8 B3, 168 L9	4.67	7,587

Table 7: ABS/CF composite material properties used in the BAAM double-wall analysis [29].

Property	ABS/CF
Density $[kg/m^3]$	1140.0
Thermal conductivity $[W/mK]$	0.17
Specific heat capacity $[J/kgK]$	1640.0
Emissivity ε	0.87
Track width (dY) [mm]	10.0
Track thickness (dZ) [mm]	4.064

3.3 Modeling of a composite double-wall

The last assessment investigates the capability of the proposed framework towards the modeling and thermal analysis of material extrusion AM of large-scale structures, i.e., those fabricated using BAAM processes. A wall-like structure is considered based on the works of Compton et al. [29], which also provides reference experimental data. The wall, as modeled, is two tracks wide and consists of 40 layers; the track width (dY) and height (dZ) are 10.0 mm and 4.064 mm, respectively. A schematic representation of the structure is shown in Fig. 13. The print material is ABS reinforced with 20% carbon fiber (ABS/CF), and its thermal properties, as suggested in [29], are listed in Table 7. The BAAM process parameters are summarized in Table 8.

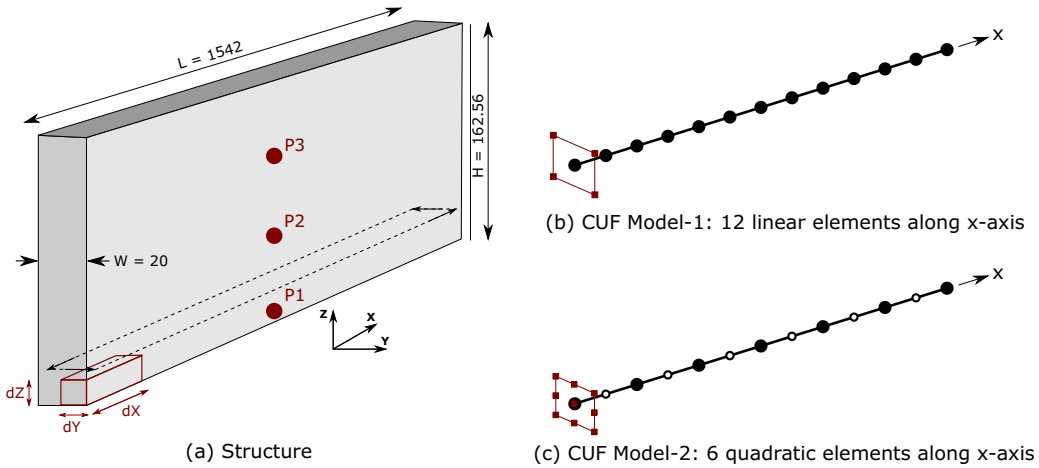

Figure 13: Schematic representation of (a) the BAAM wall (dimensions in mm). The dashed lines indicate the tool travel path within a layer, and the highlighted $dX \times dY \times dZ$ voxel domain represents an individual finite element, (b) the linear CUF model, and (c) the quadratic CUF model.

The BAAM process simulation is performed using both linear and quadratic CUF models, as shown in Fig.

Table 8: FFF process parameters used in the numerical modeling of the BAAM double-wall [29].

Parameter	ABS/CF
Extrusion temperature $[^{\circ}C]$	200.0
Chamber temperature $[^{\circ}C]$	18.0
build platform temperature $[^{\circ}C]$	65.0
Convection coefficient $[W/m^2K]$	8.5
Layer build time $[s]$	39.0

13 (b) and (c), respectively. As reported in [29], no thermal gradients were experimentally observed along the length of the wall. This observation infers a the lack of sensitivity of the model results as a function of its numerical discretization along the track direction (dX), which has been confirmed by a mesh convergence analysis not reported for the sake of brevity. As a result of the convergence study, results are presented for two types of discretization: linear (CUF - model 1, 12 elements), and quadratic (CUF - model 2, 6 elements). The thermal profile predicted by the two CUF models at the midspan of layer 1, point P1 (771.0, 20.0, 2.03); layer 15, P2 (771.0, 20.0, 58.92); and layer 30, P3 (771.0, 20.0, 119.88), have been plotted in Fig. 14. Reference experimental data from [29] and numerical simulation results based on a 2D finite volume approach [43] have also been overlaid for comparison.

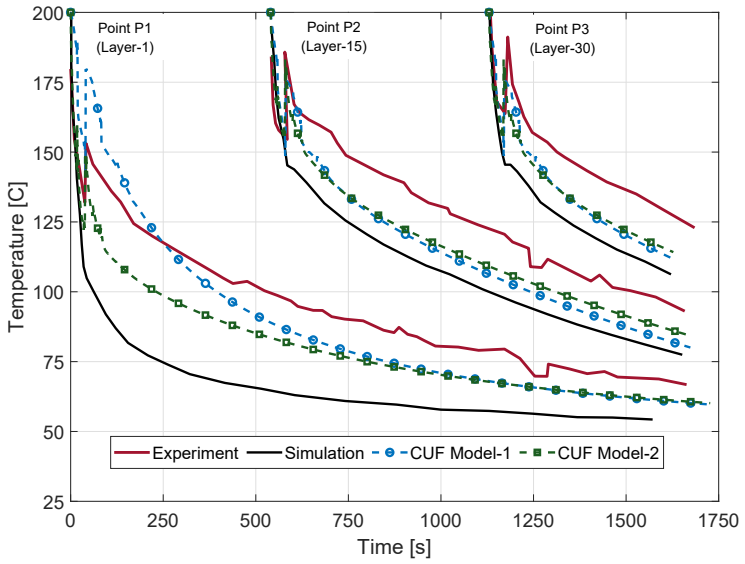

Figure 14: Thermal profile of the ABS/CF composite double-width wall (layers 1, 15, and 30) as predicted by the CUF models. Reference experimental data obtained from Compton et al. [29], and numerical simulation results from Owens et al. [43].

As seen in Fig. 14, the CUF model predictions are in qualitative agreement with the experimental curves and follow the same trend but do not correctly evaluate the temperature profile. Additionally, CUF results compare better to the experimental results than the numerical approach proposed in the original reference. The discrepancy between the experimental and numerical data likely stems from the choice of material thermal properties considered in the analysis (see Table 7, hereinafter referred to as 'nominal' values). Therefore, the

influence of the specific heat capacity C_p and thermal conductivity κ – on the thermal profile of the BAAM process model has been investigated to determine the effect of the material properties on temperature prediction.

The nominal C_p value of the ABS/CF composite has been considered 1640 J/kgK in [29]. Such a value apparently neglects the presence of the reinforcement within the thermoplastic. It is seen from Table 1 that the C_p of neat ABS is about 2100 J/kgK, while that of commercially available carbon fiber is in the range 880-1100 J/kgK [62, 63]. Assuming a general C_p value of 900 J/kgK for CF, and applying the Rule of Mixtures, the effective C_p of 20% ABS/CF is estimated to be approximately 1860 J/kgK. The sensitivity of the thermal profile between the nominal and modified C_p values, as predicted by the CUF models at Layer-15, is plotted in Fig. 15(a). Similarly, the nominal thermal conductivity κ of the ABS/CF composite is 0.17 W/mK, while that of neat ABS at elevated temperatures is generally in the range 0.19-0.20 W/mK (see Table 1). Thermally conductive reinforcements such as CF generally have transverse conductivity values over 1.0 W/mK [64]. Their presence in ABS would result in a net increase in the effective thermal conductivity, even when assuming that fibers are aligned along the extruded material, and evaluating the effective composite conductivity in the transverse direction. The effective κ of the ABS/CF composite was therefore estimated to be approximately 0.27 W/mK following the works of Bard et al. [65]. The sensitivity of the thermal profile between the nominal and modified κ values, as predicted by the CUF models at Layer-15, is plotted in Fig. 15(b).

From Fig. 15(a,b), it is seen that individually modifying C_p and κ leads to a closer agreement between the CUF predictions and the experimental data when compared to the numerical results based on nominal composite thermal properties. However, a discrepancy in the temperature values is still observed and is likely due to the modification of only a single thermal property in each analysis. Considering the modified values of both C_p and κ, the CUF predictions of the thermal profile at Layer-15 are plotted in Fig. 15(c). In this case, the CUF predictions are in excellent agreement with the experimental curves and are significantly more accurate when compared to the predictions based on nominal thermal properties. In particular, it is observed from the figure that the the quadratic CUF Model-2 is more accurate than the linear CUF Model-1. Since BAAM involves extruded tracks whose cross-sectional dimensions are an order of magnitude larger than those used in FFF, a non-negligible thermal gradient exists within the track section. The second-order expansion function used in the quadratic CUF analysis to model the track cross-section can better capture these thermal gradients than the first-order functions used in the linear model and explains the relative performance of the two CUF models.

Finally, the predicted thermal profile at layers 1, 15, and 30, considering the modified values of C_p and κ has been shown in Fig. 16. The temperature distribution within the double-wall cross-section, at its midspan, is visualized in Fig. 17 and demonstrates the thermal gradients which can exist in BAAM track cross-sections. A summary of the linear and quadratic CUF models used in the BAAM analysis is presented in Table 9. The predicted results in Fig. 16 demonstrate the capability of the proposed higher-order models in accurately simulating the BAAM process and evaluating the evolving temperature field as a function of the process conditions.

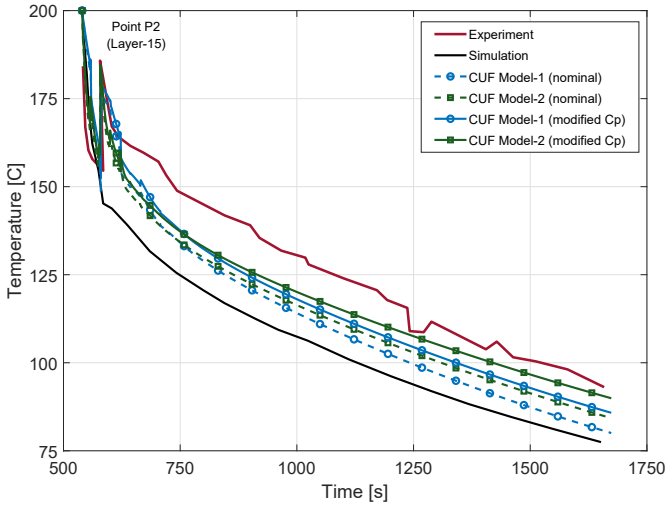

(a) Modified specific heat capacity C_p

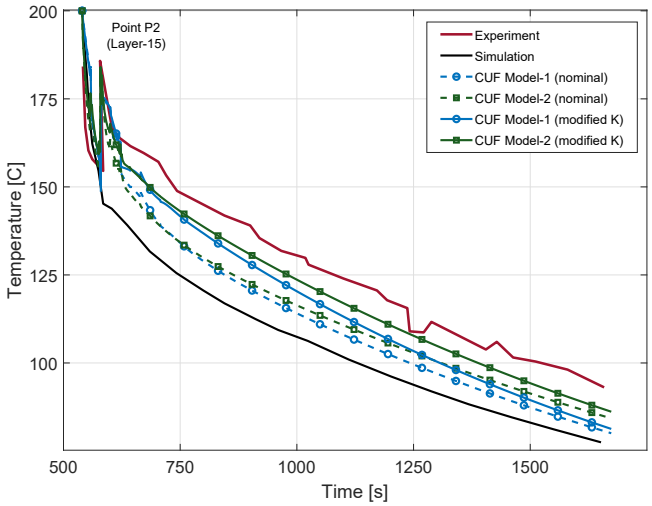

(b) Modified thermal conductivity κ

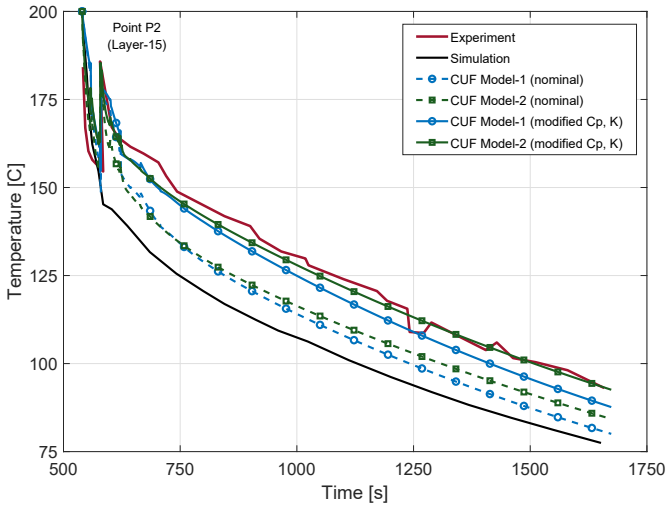

(c) Modified C_p and κ

Figure 15: Sensitivity of numerically predicted thermal profiles to variation in thermal properties.

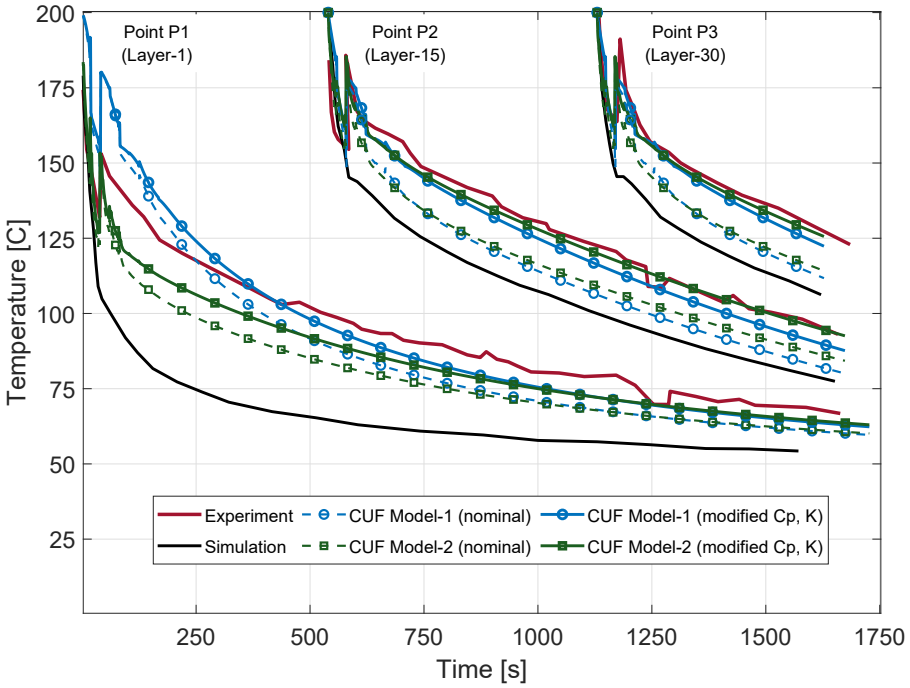

Figure 16: Thermal profile of the ABS/CF composite double-width wall (layers 1, 15, and 30) as predicted by the CUF models considering nominal and modified thermal properties. Reference experimental data obtained from Compton et al. [29], and numerical simulation results from Owens et al. [43].

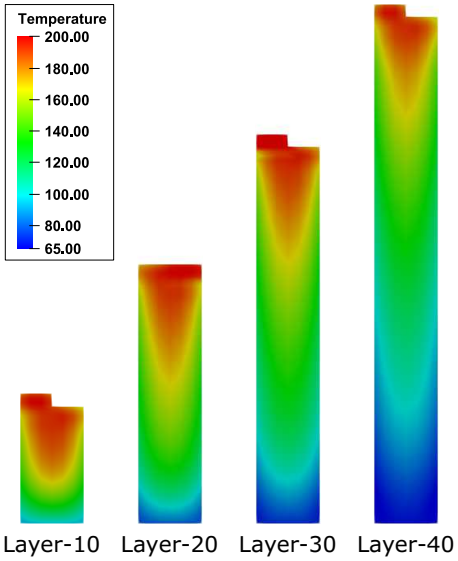

Figure 17: Temperature distribution within the midspan cross-section of the BAAM wall at various stages of print as predicted by the (quadratic) CUF Model-2.

Table 9: Summary of CUF models used in the BAAM double-width wall analysis.

Model	Discretization	Beam length (dX) [mm]	DOF
CUF Model-1 (Linear)	12 B2, 82 L4	128.5	1,638
CUF Model-2 (Quadratic)	6 B3, 82 L9	257.0	5,395

4 Conclusion

A novel numerical framework for the process modeling of material extrusion additive manufacturing is introduced in this work. The numerical model is developed using higher-order structural theories derived from the Carrera Unified Formulation and implemented within the Finite Element Method. The element activation strategy is implemented within the higher-order FE numerical framework to model the evolution of the structure during the printing process, and a transient thermal analysis is performed to evaluate the temperature field. A series of numerical assessments was carried out to evaluate the capabilities and performance of the proposed numerical framework. Process modeling simulations of a single filament-width wall and an open-box were carried out for initial verification and validation. The obtained results were in excellent agreement with experimental data, thereby validating the framework for the process modeling of material extrusion additive manufacturing. The framework's capability in modeling Big Area Additive Manufacturing was also assessed by modeling a large-scale wall. The thermal profiles predicted by the higher-order models correlated very well with the experimental data, thus validating it for BAAM process modeling applications. A sensitivity study was also performed to investigate the influence of material thermal properties on the thermal profile of the BAAM wall. The obtained results demonstrate the capabilities of the numerical framework in accurately modeling the thermal profile evolution of material extrusion additive manufacturing processes at different structural scales using higher-order finite elements, proving the potential of the proposed approach as an optimization framework to estimate favorable process parameters. Future works include extending the framework to thermo-mechanical analysis to evaluate process-induced residual stress development and distortion in AM thermoplastic parts, as well as using multiscale techniques to investigate the relation between material microstructure and manufacturing conditions.

5 Acknowledgments

This material is based upon work supported by the National Science Foundation under grant number IIP-1822147 (Phase I IUCRC at University of Massachusetts Lowell: Center for Science of Heterogeneous Additive Printing of 3D Materials (SHAP3D)) and from the SHAP3D I/UCRC Members, and National Science Foundation CAREER Award #2145387. Any opinions, findings, and conclusions or recommendations expressed in this material are those of the author(s) and do not necessarily reflect the views of the National Science Foundation or the sponsors.

References

[1] UM Dilberoglu, B Gharehpapagh, U Yaman, and M Dolen. The role of additive manufacturing in the era of industry 4.0. *Procedia Manufacturing*, 11:545–554, 2017.

[2] ISO/ASTM 52900:2021(E). Additive manufacturing — general principles — fundamentals and vocabulary. Standard, International Organization for Standardization and ASTM International, 2022.

[3] J-Y Lee, J An, and CK Chua. Fundamentals and applications of 3d printing for novel materials. *Applied materials today*, 7:120–133, 2017.

[4] SF Costa, FM Duarte, and JA Covas. Thermal conditions affecting heat transfer in fdm/ffe: a contribution towards the numerical modelling of the process. *Virtual and Physical Prototyping*, 10(1):35–46, 2015.

[5] A Cattenone, S Morganti, G Alaimo, and F Auricchio. Finite element analysis of additive manufacturing based on fused deposition modeling: distortions prediction and comparison with experimental data. *Journal of Manufacturing Science and Engineering*, 141(1), 2019.

[6] A Trofimov, J Le Pavic, S Pautard, D Therriault, and M Lévesque. Experimentally validated modeling of the temperature distribution and the distortion during the fused filament fabrication process. *Additive Manufacturing*, 54:102693, 2022.

[7] OS Es-Said, J Foyos, R Noorani, M Mendelson, R Marloth, and BA Pregger. Effect of layer orientation on mechanical properties of rapid prototyped samples. *Materials and Manufacturing Processes*, 15(1):107–122, 2000.

[8] S Sunny, H Chen, A Malik, and H Lu. Influence of residual stress and fluid–structure interaction on the impact behavior of fused filament fabrication components. *Additive Manufacturing*, 37:101662, 2021.

[9] GM Odegard, SU Patil, PP Deshpande, K Kanhaiya, JJ Winetrout, H Heinz, SP Shah, and M Maiaru. Molecular dynamics modeling of epoxy resins using the reactive interface force field. *Macromolecules*, 54(21):9815–9824, 2021.

[10] SU Patil, SP Shah, M Olaya, PP Deshpande, M Maiaru, and GM Odegard. Reactive molecular dynamics simulation of epoxy for the full cross-linking process. *ACS Applied Polymer Materials*, 3(11):5788–5797, 2021.

[11] RJ D'Mello, AM Waas, M Maiaru, and R Koon. Integrated computational modeling for efficient material and process design for composite aerospace structures. In *AIAA Scitech 2020 Forum*, page 0655, 2020.

[12] PS Gaikwad, AS Krieg, PP Deshpande, SU Patil, JA King, M Maiaru, and GM Odegard. Understanding the origin of the low cure shrinkage of polybenzoxazine resin by computational simulation. *ACS Applied Polymer Materials*, 3(12):6407–6415, 2021.

[13] S Shah, S Patil, P Deshpande, A Krieg, K Kashmari, H Al Mahmud, J King, GM Odegard, and M Maiaru. Multiscale modeling for virtual manufacturing of thermoset composites. In *AIAA Scitech 2020 Forum*, page 0882, 2020.

[14] S PATIL, S SHAH, P DESHPANDE, K KASHMARI, M OLAYA, G ODEGARD, and M MAIARU. Multiscale approach to predict cure-induced residual stresses in an epoxy system. In *Proceedings of the American Society for Composites â€" Thirty-fifth Technical Conference*, 2020.

[15] SP Shah, SU Patil, CJ Hansen, GM Odegard, and M Maiarù. Process modeling and characterization of thermoset composites for residual stress prediction. *Mechanics of Advanced Materials and Structures*, pages 1–12, 2021.

[16] SP Shah and M Maiarù. Effect of manufacturing on the transverse response of polymer matrix composites. *Polymers*, 13(15):2491, 2021.

[17] M Maiaru. Effect of uncertainty in matrix fracture properties on the transverse strength of fiber reinforced polymer matrix composites. In *2018 AIAA/ASCE/AHS/ASC Structures, Structural Dynamics, and Materials Conference*, page 1901, 2018.

[18] S SHAH and M MAIARU. Microscale analysis of virtually cured polymer matrix composites accounting for uncertainty in matrix properties during manufacturing. In *Proceedings of the American Society for Composites â€" Thirty-third Technical Conference*, 2018.

[19] A Lee, M Wynn, L Quigley, M Salviato, and N Zobeiry. Effect of temperature history during additive manufacturing on crystalline morphology of peek. *Advances in Industrial and Manufacturing Engineering*, page 100085, 2022.

[20] AC Abbott, GP Tandon, RL Bradford, H Koerner, and JW Baur. Process-structure-property effects on abs bond strength in fused filament fabrication. *Additive Manufacturing*, 19:29–38, 2018.

[21] DJ Braconnier, RE Jensen, and AM Peterson. Processing parameter correlations in material extrusion additive manufacturing. *Additive Manufacturing*, 31:100924, 2020.

[22] D Popescu, A Zapciu, C Amza, F Baciu, and R Marinescu. Fdm process parameters influence over the mechanical properties of polymer specimens: A review. *Polymer Testing*, 69:157–166, 2018.

[23] Z Hu and S Mahadevan. Uncertainty quantification and management in additive manufacturing: current status, needs, and opportunities. *The International Journal of Advanced Manufacturing Technology*, 93(5):2855–2874, 2017.

[24] P Nath, JD Olson, S Mahadevan, and Y-T Tina Lee. Optimization of fused filament fabrication process parameters under uncertainty to maximize part geometry accuracy. *Additive manufacturing*, 35:101331, 2020.

[25] GL Knapp, T Mukherjee, JS Zuback, HL Wei, TA Palmer, A De, and TJAM DebRoy. Building blocks for a digital twin of additive manufacturing. *Acta Materialia*, 135:390–399, 2017.

[26] T Debroy, W Zhang, J Turner, and SS Babu. Building digital twins of 3d printing machines. *Scripta Materialia*, 135:119–124, 2017.

[27] Y Zhang and YK Chou. Three-dimensional finite element analysis simulations of the fused deposition modelling process. *Proceedings of the Institution of Mechanical Engineers, Part B: Journal of Engineering Manufacture*, 220(10):1663–1671, 2006.

[28] Y Zhang and K Chou. A parametric study of part distortions in fused deposition modelling using three-dimensional finite element analysis. *Proceedings of the Institution of Mechanical Engineers, Part B: Journal of Engineering Manufacture*, 222(8):959–968, 2008.

[29] BG Compton, BK Post, CE Duty, L Love, and V Kunc. Thermal analysis of additive manufacturing of large-scale thermoplastic polymer composites. *Additive Manufacturing*, 17:77–86, 2017.

[30] A D'Amico and AM Peterson. An adaptable fea simulation of material extrusion additive manufacturing heat transfer in 3d. *Additive Manufacturing*, 21:422–430, 2018.

[31] Y Zhang and V Shapiro. Linear-time thermal simulation of as-manufactured fused deposition modeling components. *Journal of Manufacturing Science and Engineering*, 140(7), 2018.

[32] M Roy, R Yavari, C Zhou, O Wodo, and P Rao. Prediction and experimental validation of part thermal history in the fused filament fabrication additive manufacturing process. *Journal of Manufacturing Science and Engineering*, 141(12), 2019.

[33] T D'Amico and AM Peterson. Bead parameterization of desktop and room-scale material extrusion additive manufacturing: How print speed and thermal properties affect heat transfer. *Additive Manufacturing*, 34:101239, 2020.

[34] A Lepoivre, N Boyard, A Levy, and V Sobotka. Heat transfer and adhesion study for the fff additive manufacturing process. *Procedia manufacturing*, 47:948–955, 2020.

[35] D Xu, Y Zhang, and F Pigeonneau. Thermal analysis of the fused filament fabrication printing process: Experimental and numerical investigations. *International Journal of Material Forming*, 14(4):763–776, 2021.

[36] HR Vanaei, S Khelladi, M Deligant, M Shirinbayan, and A Tcharkhtchi. Numerical prediction for temperature profile of parts manufactured using fused filament fabrication. *Journal of Manufacturing Processes*, 76:548–558, 2022.

[37] J Zhang, B Van Hooreweder, and E Ferraris. T4f3: temperature for fused filament fabrication. *Progress in Additive Manufacturing*, pages 1–21, 2022.

[38] A El Moumen, M Tarfaoui, and K Lafdi. Modelling of the temperature and residual stress fields during 3d printing of polymer composites. *The International Journal of Advanced Manufacturing Technology*, 104(5):1661–1676, 2019.

[39] N Dialami, M Chiumenti, M Cervera, R Rossi, U Chasco, and M Domingo. Numerical and experimental analysis of the structural performance of am components built by fused filament fabrication. *International journal of mechanics and materials in design*, 17(1):225–244, 2021.

[40] C Ajinjeru, V Kishore, P Liu, J Lindahl, AA Hassen, V Kunc, B Post, L Love, and C Duty. Determination of melt processing conditions for high performance amorphous thermoplastics for large format additive manufacturing. *Additive Manufacturing*, 21:125–132, 2018.

[41] P Chesser, B Post, A Roschli, C Carnal, R Lind, M Borish, and L Love. Extrusion control for high quality printing on big area additive manufacturing (baam) systems. *Additive Manufacturing*, 28:445–455, 2019.

[42] K Choo, B Friedrich, T Daugherty, A Schmidt, C Patterson, MA Abraham, B Conner, K Rogers, P Cortes, and E MacDonald. Heat retention modeling of large area additive manufacturing. *Additive Manufacturing*, 28:325–332, 2019.

[43] JT Owens, A Das, and MJ Bortner. Accelerating heat transfer modeling in material extrusion additive manufacturing: From desktop to big area. *Additive Manufacturing*, 55:102853, 2022.

[44] M Roy and O Wodo. Data-driven modeling of thermal history in additive manufacturing. *Additive Manufacturing*, 32:101017, 2020.

[45] E Carrera, M Cinefra, M Petrolo, and E Zappino. *Finite element analysis of structures through unified formulation*. John Wiley & Sons, 2014.

[46] AG De Miguel, I Kaleel, MH Nagaraj, A Pagani, M Petrolo, and E Carrera. Accurate evaluation of failure indices of composite layered structures via various fe models. *Composites Science and Technology*, 167:174–189, 2018.

[47] MH Nagaraj, I Kaleel, E Carrera, and M Petrolo. Nonlinear analysis of compact and thin-walled metallic structures including localized plasticity under contact conditions. *Engineering Structures*, 203:109819, 2020.

[48] MH Nagaraj, J Reiner, R Vaziri, E Carrera, and M Petrolo. Progressive damage analysis of composite structures using higher-order layer-wise elements. *Composites Part B: Engineering*, 190:107921, 2020.

[49] MH Nagaraj, Johannes Reiner, R Vaziri, E Carrera, and M Petrolo. Compressive damage modeling of fiber-reinforced composite laminates using 2d higher-order layer-wise models. *Composites Part B: Engineering*, 215:108753, 2021.

[50] MH Nagaraj, E Carrera, and M Petrolo. Progressive damage analysis of composite laminates subjected to low-velocity impact using 2d layer-wise structural models. *International Journal of Non-Linear Mechanics*, 127:103591, 2020.

[51] MH Nagaraj and M Maiaru. Micro-scale process modeling and evaluation of curing-induced residual stresses in fiber-reinforced polymers using higher-order fe models. In *PROCEEDINGS OF THE AMERICAN SOCIETY FOR COMPOSITES-THIRTY-SEVENTH TECHNICAL CONFERENCE*, 2022.

[52] E Carrera, M Petrolo, MH Nagaraj, and M Delicata. Evaluation of the influence of voids on 3d representative volume elements of fiber-reinforced polymer composites using cuf micromechanics. *Composite Structures*, 254:112833, 2020.

[53] M Petrolo, MH Nagaraj, I Kaleel, and E Carrera. A global-local approach for the elastoplastic analysis of compact and thin-walled structures via refined models. *Computers & Structures*, 206:54–65, 2018.

[54] MH Nagaraj, M Petrolo, and E Carrera. A global–local approach for progressive damage analysis of fiber-reinforced composite laminates. *Thin-Walled Structures*, 169:108343, 2021.

[55] MH Nagaraj, E Carrera, and M Petrolo. A global-local approach to the high-fidelity impact analysis of composite structures based on node-dependent kinematics. *Composite Structures*, page 116307, 2022.

[56] E Carrera, M Maiaru, M Petrolo, and G Giunta. A refined 1d element for the structural analysis of single and multiple fiber/matrix cells. *Composite Structures*, 96:455–468, 2013.

[57] M Maiaru, M Petrolo, and E Carrera. Evaluation of energy and failure parameters in composite structures via a component-wise approach. *Composites Part B: Engineering*, 108:53–64, 2017.

[58] Y Zhou, H Lu, G Wang, J Wang, and W Li. Voxelization modelling based finite element simulation and process parameter optimization for fused filament fabrication. *Materials & Design*, 187:108409, 2020.

[59] K-J Bathe and MR Khoshgoftaar. Finite element formulation and solution of nonlinear heat transfer. *Nuclear Engineering and Design*, 51(3):389–401, 1979.

[60] A. Entezari, M. Filippi, and E. Carrera. Unified finite element approach for generalized coupled thermoelastic analysis of 3d beam-type structures, part 1: Equations and formulation. *Journal of Thermal Stresses*, 40(11):1386–1401, 2017.

[61] J Zhang, E Vasiliauskaite, A De Kuyper, C De Schryver, F Vogeler, F Desplentere, and E Ferraris. Temperature analyses in fused filament fabrication: from filament entering the hot-end to the printed parts. *3D Printing and Additive Manufacturing*, 9(2):132–142, 2022.

[62] Hexcel. *HexTow ® IM7 Carbon Fiber Product Data Sheet.*

[63] Hexcel. *HexTow ® AS4 Carbon Fiber Product Data Sheet.*

[64] M Villière, D Lecointe, V Sobotka, N Boyard, and D Delaunay. Experimental determination and modeling of thermal conductivity tensor of carbon/epoxy composite. *Composites Part A: Applied Science and Manufacturing*, 46:60–68, 2013.

[65] S Bard, F Schönl, M Demleitner, and V Altstädt. Influence of fiber volume content on thermal conductivity in transverse and fiber direction of carbon fiber-reinforced epoxy laminates. *Materials*, 12(7):1084, 2019.